ISSN 1063-7710, Acoustical Physics, 2026, Vol. 72, No. 1, pp. 14–28. © Pleiades Publishing, Ltd., 2026.

NONLINEAR ACOUSTICS

Feasibility of Achieving Shock-Wave Focusing Regimes Using High-Frequency Miniature Ultrasound Sources

M. M. Karzova[a], *, L. A. Papikyan[a], and V. A. Khokhlova[a]

[a] *Lomonosov Moscow State University, Faculty of Physics, Moscow, 119991 Russia*

**e-mail: masha@acs366.phys.msu.ru*

Received December 4, 2025; revised December 4, 2025; accepted January 29, 2026

Abstract—Current high-intensity focused ultrasound (HIFU) methods primarily target biological tissue at depths of several centimeters, utilizing frequencies in the 0.7–2 MHz range. Of particular interest are nonlinear operational regimes, in which the wave profile within the ultrasound transducer's focal region contains high-amplitude shock fronts. These regimes significantly broaden the spectrum of bioeffects achievable through ultrasound exposure. Shock-wave regimes hold great promise for the selective treatment of superficial skin layers at millimeter-scale depths. This approach requires increasing the ultrasound frequency to 4–10 MHz and developing miniature transducers with diameters of 15–20 mm. However, the feasibility of generating shock fronts with such transducers at relatively modest power levels (~100 W), attainable under practical conditions, has not yet been studied. In this work, numerical modeling was conducted to investigate this problem. The results demonstrate that shock front amplitudes up to 130 MPa can be achieved at the focus in skin tissue at input powers below 120 W using 4 MHz transducers with a diameter of 20 mm and a radius of curvature between 16 and 20 mm. Similarly, at 7 MHz, equivalent effects can be produced with comparable transducer parameters and input powers of less than 40 W. These findings suggest the feasibility of implementing shock wave-based methods for superficial skin treatments—such as those used in aesthetic medicine, dermatology, and plastic surgery—for scar tissue treatment—as well as in various other clinical contexts.

Keywords: high-intensity focused ultrasound, HIFU, skin, cosmetology, miniature transducers, shock front, numerical modeling

DOI: 10.1134/S1063771025601268

INTRODUCTION

Modern medicine prioritizes the development of minimally invasive and noninvasive surgical techniques that reduce the risk of infection, minimize collateral tissue damage, and accelerate patient recovery after surgery. High-intensity focused ultrasound (HIFU) is a promising noninvasive modality with a broad range of clinical applications [1–5].

HIFU focuses an ultrasound beam from outside the human body onto a targeted region at a specific depth, exerting a localized therapeutic effect while preserving the integrity of intervening tissues located between the transducer and the focal region. Modern HIFU methods are used primarily for tissue exposures at frequencies of 0.7–2 MHz and depths of several centimeters. In clinical practice, HIFU has already been used to treat various pathologies: neurological diseases of the brain (essential tremor, Parkinson's disease, dystonia), malignant tumors of various organs (liver, prostate, pancreas, breast, and thyroid glands), uterine fibroids, as well as for targeted drug delivery and palliative care for metastases [1, 4].

Current clinical HIFU systems primarily induce thermal effects in the target tissue. The absorption of ultrasound wave energy leads to tissue heating in the focal region to temperatures >70°C for 1–3 s, which is sufficient for denaturation of cellular structures and the formation of local thermal necrosis [4, 5]. In such approach, linear or quasi-linear ultrasound focusing regimes are used, when the intensity of the wave at the focus does not exceed several hundred W/cm^2, and the wave profile remains almost harmonic [5–7].

However, recently there has been growing interest in using regimes characterized by strong nonlinear acoustic effects, in which shock fronts form in the wave profile at the focus of the transducer. It has been shown that such regimes significantly expand the range of possible bioeffects induced by ultrasound [2, 3]. Specifically, pulse-periodic exposures with a sufficiently low duty cycle, focal high intensities exceeding 10 kW/cm^2, and micro- or millisecond pulse durations generate high-amplitude shock fronts in the focal wave profile that mechanically disintegrate tissue down to subcellular debris. This approach is termed histotripsy (from the Greek "histos"—tissue, "tribein"—to crush). The physical mechanisms of his-

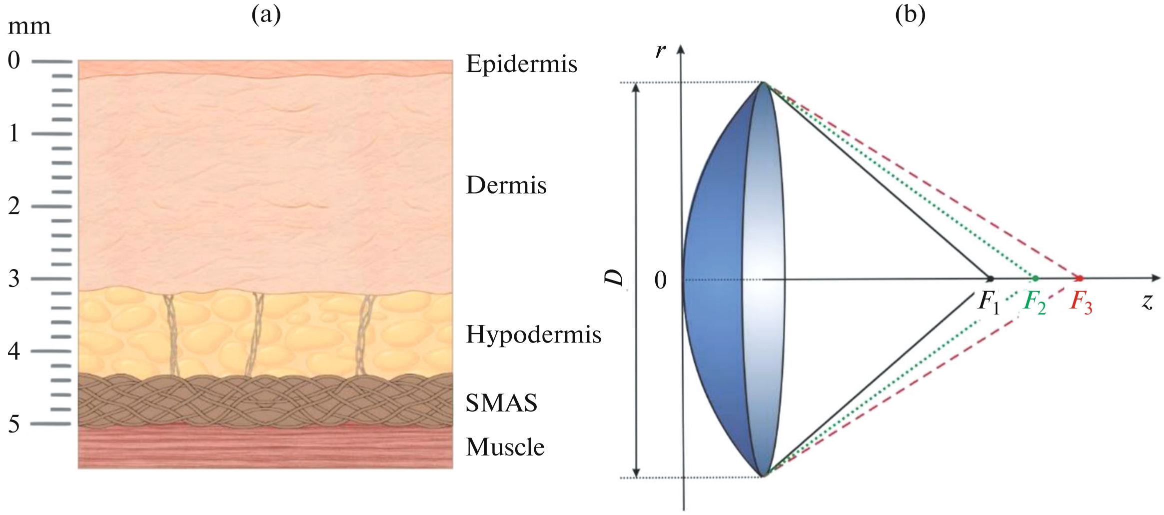

Fig. 1. (a) Schematic representation of skin structure. (b) Diagram of the problem: spherical transducer with uniform distribution of vibrational velocity over its surface and aperture $D = 20$ mm focuses ultrasonic field into water. Three transducers with different focusing depths are considered: $F_1 = 16$ mm, $F_2 = 18$ mm, and $F_3 = 20$ mm. F-numbers, $F\# = F/D$, are 0.8, 0.9, and 1.0, respectively. Operating frequencies $f_1 = 4$ and $f_2 = 7$ MHz are investigated.

totripsy are quite complex. They include ultra-fast localized boiling of tissue due to the effective absorption of ultrasonic wave energy at the shock fronts (boiling histotripsy) [8, 9], as well as the formation of a dense cavitation cloud due to the interaction of shock fronts with vapor-gas cavities or spontaneously formed primary cavitation microbubbles. This interaction subsequently leads to formation of microjets and tissue atomization [2, 3, 10]. Under sustained shock-wave exposure, the efficiency of the thermal effect on tissue increases significantly, accompanied by the formation of vapor-gas cavities within the focal region [11–13]. An important clinical advantage of both histotripsy and thermal HIFU with boiling is the ability to monitor them in real time using conventional diagnostic ultrasound, leveraging the high echogenicity of the bubbles formed within the focal zone.

Shock wave focusing regimes have already been successfully implemented in laboratory and clinical settings for exposures at traditional HIFU depths of several centimeters and frequencies of 0.7–2 MHz [6, 14–16]. Their application is also highly promising for the selective irradiation of superficial skin layers located at depths of up to several millimeters. This requires increasing the ultrasound frequency to 4–10 MHz and utilizing miniature transducers with a diameter of 15–20 mm. However, the feasibility of generating shock fronts at the focus of such transducers at relatively low power levels (on the order of 100 W), achievable under practical conditions, remains unresolved [17].

Miniature transducers are of particular interest, especially those used in dermatology and aesthetic medicine for lifting (tightening) the skin of the face and neck, lipolysis (breakdown of fat cells), reducing wrinkles, and treating hyperhidrosis and hyperpigmentation [18, 19]. Human skin (Fig. 1a) anatomically consists of three main layers: the epidermis (~0.1 mm), dermis (up to 3–4 mm), and hypodermis, which is also called subcutaneous fat [20]. Between the hypodermis and deep facial muscles, at a depth of approximately 3–4.5 mm, is the superficial musculoaponeurotic system (SMAS), formed of muscle, collagen, and elastin fibers responsible for firmness and elasticity of the skin [21, 22]. Ultrasonic lifting focuses ultrasound energy into sub-epidermal layers, inducing localized thermal denaturation of collagen fibers and stimulating neocollagenesis within coagulation zones, while leaving surrounding tissues intact [17, 23–25].

Typically, transducers operating at 4, 6–7, and 10 MHz frequencies are used for exposures at target depths of 4.5, 3.0, and 1.5 mm, respectively. Sequential application of these transducers stimulates neocollagenesis through the tissue volume, extending from the SMAS layer to the superficial dermis [18]. Currently, the following clinical systems are widely used for skin tightening: Ulthera (Merz North America, Inc), Ultraformer (Classys, Inc, Seoul, Korea), Liftera (ASTERASYS Co., Ltd, Seoul, Korea), etc. The choice of a specific system is determined by clinical indications and individual characteristics of the patient [26]. Beyond cosmetology, the use of miniature transducers and shock wave regimes has strong potential for treating melanomas, scars, and diseases accompanied by the formation of scar tissue, such as Dupuytren's contracture [27, 28]. This contracture is characterized by the proliferation of dense connective tissue, leading to a restricted range of motion or complete loss of joint mobility. Currently, noninvasive methods of treating contracture can only slow down the progression of the disease [29, 30]. Creating a network of single thermal or mechanical lesions in scar tissue with ultrasound real-time guidance of the sonication can facilitate adhesion remodeling and restore mobility to the affected joint.

The aim of this article was to numerically investigate the feasibility of implementing shock-wave focusing regimes in the fields of miniature high-frequency ultrasonic transducers at relatively low power levels achievable under practical conditions.

FORMULATION OF THE PROBLEM

Numerical modeling methods were used to simulate physical experiments aimed at characterizing the focused ultrasonic field in water under a gradual increase in the acoustic output power of the transducer. Three spherical ultrasound sources with a uniform distribution of vibrational velocity over their surfaces were considered. The aperture diameter of the transducers was $D = 20$ mm, and the focal lengths (radii of curvature of the active surface) were $F_1 = 16$ mm, $F_2 = 18$ mm, and $F_3 = 20$ mm (Fig. 1b). The corresponding F-numbers ($F\#$), defined as the ratio of the focal length of the transducer to its aperture, $F\# = F/D$, were 0.8, 0.9 and 1.0, respectively. For each of the three transducers, operating frequencies $f_1 = 4$ MHz and $f_2 = 7$ MHz were considered. As indicated above, the selected parameters of the transducers are characteristic of miniature, high-frequency focused ultrasound sources used in aesthetic medicine and other treatments of the superficial layers of biological structures [27, 29].

The aim of the study was to determine the ranges of acoustic power values for each of the transducers, at which shock fronts are formed at the focus. The spatiotemporal structure of the acoustic fields of the transducers was analyzed across focusing regimes characterized by varying degrees of nonlinear waveform distortion at the focus. First, the dimensions of the focal region and the pressure gains at the focus were analyzed in the linear focusing regime. Then, three power thresholds were determined [7], corresponding to the following nonlinear focusing regimes:

(1) Quasi-linear waveform distortion at the focus, where 10% of the acoustic intensity is converted into higher harmonics;

(2) The formation of a fully developed shock in the focal waveform, representing the most effective nonlinear focusing regime, where the ratio of the pressure jump A_s at the shock front in the focal waveform to the initial pressure amplitude p_0 on the transducer reaches its maximum;

(3) Saturation of the peak positive pressure p_+ at the focus, defined as the point on the $p_+(p_0)$ curve where the derivative of the curve decreases to 10% of its value at the fully developed shock threshold.

For these three characteristic nonlinear regimes, which differ in the severity of nonlinear effects, the pressure waveforms at the focus were analyzed. Furthermore, the spatial distributions, dimensions, and shapes of the focal regions are determined for both peak positive p_+ and negative p_- pressures, along with the shock-front pressure jump A_s at the focus. Additionally, the dependences of the peak positive pressure p_+, peak negative pressure p_-, and the shock amplitude A_s at the focus on the initial pressure amplitude p_0 at the transducer were calculated. Simulations were conducted for focusing in water, and the corresponding in situ parameters were then estimated for a two-layer water–skin structure using the nonlinear derating method [9, 31].

THEORETICAL AND NUMERICAL MODELS

Acoustic Field in Water

The focusing of the ultrasonic beam in water is described by the unidirectional Westervelt equation, which accounts for nonlinear and diffraction effects as well as thermoviscous absorption [32]:

$$\frac{\partial^2 p}{\partial\tau\partial z} = \frac{c_0}{2}\left(\frac{\partial^2 p}{\partial z^2} + \frac{\partial^2 p}{\partial r^2} + \frac{1}{r}\frac{\partial p}{\partial r}\right) + \frac{\beta}{2\rho_0 c_0^3}\frac{\partial^2 p^2}{\partial\tau^2} + \frac{\delta}{2c_0^3}\frac{\partial^3 p}{\partial\tau^3}, \quad (1)$$

where $p = p(r, z, \tau)$ is the pressure, z is the coordinate along the beam axis, r is the radial coordinate perpendicular to the axis z, $\tau = t - z/c_0$ is the retarded time, t is the time, and the parameters c_0, β, ρ_0, and δ are the speed of sound, the nonlinearity coefficient, the ambient density, and the coefficient of thermoviscous absorption in the medium, respectively. The values of the specified physical parameters correspond to the parameters of water at a temperature of 21°C and were $c_0 = 1485.4$ m/s, $\beta = 3.5$, $\rho_0 = 997.4$ kg/m^3, and $\delta = 4.33 \times 10^{-6}$ m^2/s [33].

Numerical simulations of Eq. (1) were performed using the open-access software package "HIFU Beam" in the WAPE mode, which is based on a wide-angle approximation of the diffraction operator [34]. The numerical mesh parameters used in the calculations were selected as follows: number of harmonics $N_h = 1000$; the step along the axial coordinate $dz = 2.5 \times 10^{-2}$ mm; the step along the transverse coordinate decreased with increasing transducer power to saturation regimes from $dr = 1 \times 10^{-2}$ mm for transducers with a frequency of 4 MHz and $dr = 5 \times 10^{-3}$ mm for transducers with a frequency of 7 MHz up to $dr = 5 \times 10^{-3}$ mm and $dr = 5 \times 10^{-4}$ mm, respectively; the dimensions of the spatial numerical window were [0–2.56] cm in the transverse direction r and [0–2] cm in the axial direction z.

A Derating Method for Estimating Acoustic Field Parameters in Biological Tissue

To determine the acoustic field parameters in the layered water–skin structure, the nonlinear derating method was used [9, 34]. Based on the known parameters of the nonlinear acoustic field in water, this method enables the estimation of the corresponding in situ field parameters in biological tissue with different absorption, nonlinearity, sound speed, and density.

For HIFU transducers, the derating method relies on the pressure magnitude in the focal region being significantly higher than in the prefocal region, with the focal region length being much shorter than the focal length of the transducer. Under such conditions, nonlinear effects in the focal region of the beam dominate over those occurring during propagation to the focus. In addition, the degree of nonlinear waveform distortion at the focus is governed primarily by the pressure level in the focal region and the combination of the values of nonlinearity parameter, speed of sound, and density. Therefore, given identical values of the nonlinear parameter β, sound speed c_0, and density ρ_0 of the medium, scaling the source pressure amplitude on the transducer $p_{0\text{tissue}}$ (or its power $W_{0\text{tissue}}$) to compensate for tissue absorption at a given depth ensures that the resulting nonlinearly distorted focal waveforms in water and in tissue are nearly identical in both shape and peak pressure values:

$$\begin{gathered} p_{0\text{tissue}} = p_{0\text{water}} \exp(\alpha L), \\ W_{0\text{tissue}} = W_{0\text{water}} \exp(2\alpha L), \quad p_{\text{F tissue}} = p_{\text{F water}}, \end{gathered} \tag{2}$$

where α is the ultrasound absorption coefficient in tissue at the operating frequency, L is the depth of wave focusing in the tissue, p_F is the pressure at the focus. In other words, the acoustic field parameters at the focus in the tissue under the corrected initial conditions $p_{0\text{tissue}}$ and $W_{0\text{tissue}}$ (2) are nearly identical to those in water under the initial conditions $p_{0\text{water}}$ and $W_{0\text{water}}$ [34].

To account for the different nonlinearity parameters β of water and tissue, the method relies on the fact that the dimensionless solutions to Eq. (1) in the absence of absorption are identical for identical values of the dimensionless parameter $N = 2\pi F f \beta p_0 / (\rho_0 c_0^3)$, which is proportional to the product of the initial pressure amplitude p_0 and the nonlinearity coefficient β [9]. In this case, to account for the different manifestations of nonlinear effects, the parameters $p_{0\text{tissue}}$ and $W_{0\text{tissue}}$ are scaled as follows [9]:

$$\begin{gathered} p_{0\text{tissue}} = p_{0\text{water}} \frac{\beta_\text{water}}{\beta_\text{tissue}}, \quad W_{0\text{tissue}} = W_{0\text{water}} \left(\frac{\beta_\text{water}}{\beta_\text{tissue}}\right)^2, \\ p_{\text{F tissue}} = p_{\text{F water}} \frac{\beta_\text{water}}{\beta_\text{tissue}}. \end{gathered} \tag{3}$$

In this article, the derating method also accounts for the differences in the medium properties c_0 and ρ_0 between water and tissue. Since the dimensionless parameter N includes the speed of sound c_0 and the density of the medium ρ_0 as the combination $p_0/(\rho_0 c_0^3)$, in the absence of absorption and for identical nonlinear parameters β, the scaling of $p_{0\text{tissue}}$ and $W_{0\text{tissue}}$ is carried out as follows:

$$\begin{gathered} p_{0\text{tissue}} = p_{0\text{water}} \frac{(\rho_0 c_0^3)_\text{tissue}}{(\rho_0 c_0^3)_\text{water}}, \\ W_{0\text{tissue}} = W_{0\text{water}} \frac{(\rho_0 c_0^3)^2_\text{tissue}}{(\rho_0 c_0^3)^2_\text{water}}, \\ p_{\text{F tissue}} = p_{\text{F water}} \frac{(\rho_0 c_0^3)_\text{tissue}}{(\rho_0 c_0^3)_\text{water}}. \end{gathered} \tag{4}$$

Accounting for the differences in absorption, nonlinearity, sound speed, and density between water and tissue enables the estimation of the initial amplitude at the transducer and its power. These estimates ensure that focusing in tissue replicates the dimensionless nonlinear field parameters obtained in water. Then, according to Eqs. (2)–(4), the conversion of the acoustic field parameters from water to tissue can be carried out using the formulas:

$$\begin{gathered} p_{0\text{tissue}} = p_{0\text{water}} \exp(\alpha L) \frac{\left(\beta/(\rho_0 c_0^3)\right)_\text{water}}{\left(\beta/(\rho_0 c_0^3)\right)_\text{tissue}}, \\ W_{0\text{tissue}} = W_{0\text{water}} \exp(2\alpha L) \frac{\left(\beta/(\rho_0 c_0^3)\right)^2_\text{water}}{\left(\beta/(\rho_0 c_0^3)\right)^2_\text{tissue}}, \\ p_{\text{F tissue}} = p_{\text{F water}} \frac{\left(\beta/(\rho_0 c_0^3)\right)_\text{water}}{\left(\beta/(\rho_0 c_0^3)\right)_\text{tissue}}. \end{gathered} \tag{5}$$

To estimate the *in situ* acoustic field parameters at the focus using the nonlinear derating method (5), the tabulated acoustic parameters of skin were used: α = 21.158 Np/m/MHz, c_0 = 1624 m/s, β = 4.9, ρ_0 = 1109 kg/m^3 [35, 36]. Thus, when focusing in the skin at a depth of L = 3 mm and a frequency of f = 7 MHz, the power correction factor associated with higher absorption in the medium is $\exp(2\alpha L)$ = 2.43, and for a depth of L = 4.5 mm and a frequency of f = 4 MHz, the corresponding factor decreases to $\exp(2\alpha L)$ = 2.14. In this case, when scaling the power values, the coefficient associated with the difference in the parameters β, c_0 and ρ_0 is $\left(\beta/\left(\rho_0 c_0^3\right)\right)^2_{\text{water}}\Big/\left(\beta/\left(\rho_0 c_0^3\right)\right)^2_{\text{tissue}} = 1.08$, which is less significant than the correction factor associated with absorption. Notably, accounting only for the difference in the nonlinearity coefficients β according to formula (3) reduces the shock amplitude at the focus in tissue by 30% compared to the value in water, since $\beta_{\text{water}}/\beta_{\text{tissue}} = 0.71$. However, the difference in sound speed c_0, which is 10% higher in the skin than in water, plays a significant role. Conversely, taking this difference into account increases the focal pressure magnitude in tissue compared to the value in water. Thus, the joint consideration of the differences in parameters α, β, c_0, and ρ_0 between water and skin ensures that the absorption factor remains dominant in the derating relations of Eq. (5).

RESULTS

Characteristics of Linear Acoustic Beams in Water

Figure 2 shows the spatial pressure amplitude distributions, normalized to their focal values, for the linear focusing of an ultrasound beam in water. For the transducers with an operating frequency of $f_1 = 4$ MHz (Figs. 2a, 2b), used in aesthetic applications for exposures in the skin down to depths of 4–5 mm, the dimensions of the focal region at the –6 dB level range from 2.0 mm ($F\# = 0.8$) to 3.3 mm ($F\# = 1.0$) along the beam axis and from 0.41 mm ($F\# = 0.8$) to 0.52 mm ($F\# = 1.0$) in the transverse direction, respectively. When the operating frequency is increased to $f_2 = 7$ MHz (Figs. 2c, 2d), used for exposures in the skin at depths of 1.5–3.0 mm, the corresponding dimensions of the focal region decrease by a factor of $f_2/f_1 = 1.75$. Specifically, the lengths of the focal region along the beam axis are 1.2 mm ($F\# = 0.8$) and 1.9 mm ($F\# = 1.0$), and the widths in the transverse direction are 0.23 mm ($F\# = 0.8$) and 0.3 mm ($F\# = 1.0$), respectively.

The focal regions of the pressure amplitude in the linear ultrasound beam exhibit a characteristic shape of a grain of rice (Fig. 3), while the pressure amplitude gains at the focus relative to their initial values at the surface of the transducer are 58.4, 50.5, and 44.5 for an operating frequency of $f_1 = 4$ MHz and focal lengths of $F_1 = 16$ mm, $F_2 = 18$ mm, and $F_3 = 20$ mm, respectively (Figs. 3a–3c). With an increase in the operating frequency to $f_2 = 7$ MHz, the corresponding gains increase by a factor of $f_2/f_1 = 1.75$ times: 100.9, 87.0, and 76.6 (Figs. 3d–3f).

The parameters of the acoustic field generated by the modeled transducers when focusing in water are given in Table 1.

Characteristics of Nonlinear Acoustic Beams in Water

Figure 4 shows the characteristic dependences of the peak positive p_+ and negative p_- pressures, as well as the shock amplitude A_s in the focal waveform on the initial pressure amplitude p_0 and initial wave intensity I_0 at the transducer. Note that the initial power of the ultrasound beam W_0 (Table 1), corresponding to different severity levels of nonlinear effects, is determined from the I_0 values shown in Fig. 4 by multiplying them by the active area of the transducer. The slight difference in the active area of the modeled transducers with identical apertures (see Table 1) is due to their different radii of curvature.

As can be seen from Fig. 4, the initial linear dependence of the peak positive pressure p_+ on the initial pressure amplitude p_0 is replaced by a steeper growth associated with the enhanced focusing of generated higher harmonics and their mutual phase shifts; subsequently, this growth slows down significantly due to the effective absorption of wave energy at the resulting shock fronts [6, 7]. As a result, the peak positive pressure p_+ at the focus saturates. In contrast, the peak negative pressure p_- approaches saturation monotonically, with the growth of its absolute value gradually slowing down.

Numerical simulations show (Fig. 4) that the threshold for quasi-linear waveform distortion at the focus is achieved at an operating frequency of $f_1 = 4$ MHz and focal lengths of 20, 18, and 16 mm at power levels of 4.1, 5.1, and 6.3 W, respectively (Fig. 4a). A similar threshold for the higher frequency of $f_2 = 7$ MHz is observed at even lower power levels: 1.07, 1.28, and 1.6 W, respectively (Fig. 4b), decreasing inversely proportionally to the square of the frequency ratio. In the quasi-linear regime, the peak positive pressures at the focus are 12.5, 15.8, 20 MPa for the operating frequency of $f_1 = 4$ MHz (Fig. 4a) and focal lengths of 20, 18, and 16 mm. Corresponding values for $f_2 = 7$ MHz are approximately 15% lower than the specified values due to stronger absorption at high frequencies (see Table 1).

The fully developed shock formation threshold is achieved for the operating frequency of $f_1 = 4$ MHz (Fig. 4a) and focal lengths of 20, 18, and 16 mm with corresponding transducer powers of 34.4, 41.7, and 50.3 W. Note that for the higher frequency of $f_2 = 7$ MHz (Fig. 4b), much lower powers are required: 9.6, 11.9 and 14.6 W. These values, taking into account the correction for stronger absorption, are inversely proportional to the square of the frequency ratio. The corresponding amplitudes of the fully developed shock for the operating frequency of $f_1 = 4$ MHz are 78.5, 98.7, and 126 MPa and are slightly lower (76.7, 96.3, and 123.2 MPa) for $f_2 = 7$ MHz. Thus, to achieve shock-wave focusing regimes in water with the characteristic amplitude of a fully developed shock, minia-

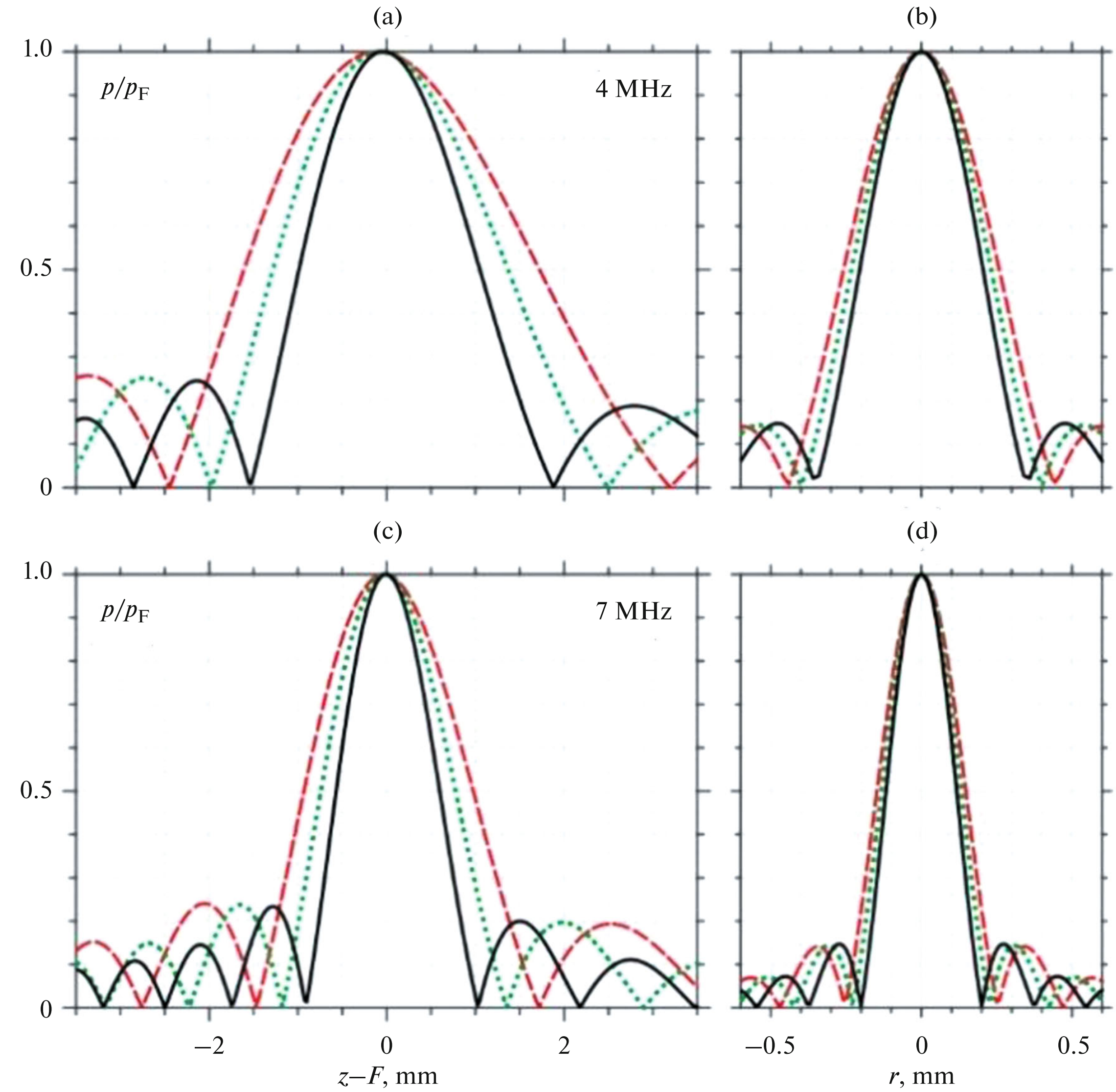

Fig. 2. Pressure amplitude distributions in the linear beam, normalized to their focal values, (a,c) along the beam axis z and (b, d) in the transverse direction r in the focal plane for frequencies (a, b) 4 and (c, d) 7 MHz. Solid curves correspond to the transducer with a focal length of F_1 = 16 mm; dotted curves, F_2 = 18 mm; and dashed curves, F_3 = 20 mm.

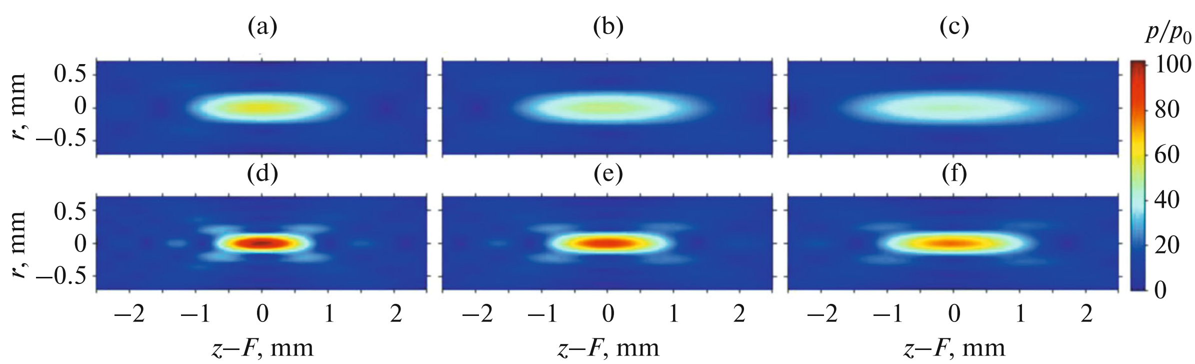

Fig. 3. Spatial distributions of the pressure amplitude, normalized to the initial amplitude p_0 at the transducer, in the axial plane of the linear beam for transducers with operating frequencies (a–c) 4 and (d–f) 7 MHz, for focusing in water at depths (a, d) F_1 = 16 mm, (b, e) F_2 = 18 mm, and (c, f) F_3 = 20 mm.

Table 1. Acoustic field parameters of the modeled transducers for linear and nonlinear focusing in water

Frequency f, MHz	4			7		
Focal length F, mm	20	18	16	20	18	16
$F\#$	1	0.9	0.8	1	0.9	0.8
Transducer area, mm^2	336.7	343.1	352.9	336.7	343.1	352.9
Color of curves	Red	Green	Black	Red	Green	Black
Gain p_F/p_0 at focus	44.5	50.5	58.4	76.6	87.0	100.9
Dimensions of focal region along axes $z \times r$, mm (level –6 dB)	3.3 × 0.52	2.7 × 0.46	2.0 × 0.41	1.9 × 0.30	1.5 × 0.26	1.2 × 0.23
Quasi-linear regime of wave profile distortion at focus (10% of wave intensity in higher harmonics)						
p_0, MPa	0.19	0.21	0.23	0.097	0.105	0.116
I_0, W/cm^2	1.22	1.49	1.79	0.318	0.372	0.454
W_0, W	4.1	5.1	6.3	1.07	1.28	1.60
p_+/p_-, MPa in focus	12.5/–6.7	15.8/–8.3	20/–10.6	11/–5.9	13.5/–7.2	17.3/–9.2
Dimensions of focal region p_+/p_- along axes $z \times r$ in mm, level –6 dB	2.7 × 0.4/ 3.7 × 0.58	2.1 × 0.36/ 3.0 × 0.54	1.6 × 0.32/ 2.3 × 0.46	1.51 × 0.23/ 2.2 × 0.34	1.23 × 0.21/ 1.72 × 0.29	0.93 × 0.19/ 1.33 × 0.26
Regime of forming a fully developed shock at focus ($p = A_s$, 50% of wave intensity in higher harmonics)						
p_0, MPa	0.55	0.6	0.65	0.29	0.32	0.35
I_0, W/cm^2	10.2	12.2	14.3	2.84	3.46	4.13
W_0, W	34.4	41.7	50.3	9.6	11.9	14.6
$p\ (=A_s)/\ p_-$, MPa in focus	78.5/–14.3	98.7/–17.5	126/–22	76.7/–12.6	96.3/–15.6	123.2/–19.8
Dimensions of focal region p_+/p_- along axes $z \times r$ in mm, level –6 dB	2.1 × 0.22/ 4.2 × 0.66	1.7 × 0.2/ 3.3 × 0.59	1.3 × 0.18/ 2.6 × 0.54	1.16 × 0.12/ 2.48 × 0.39	0.93 × 0.11/ 1.98 × 0.35	0.70 × 0.10/ 1.52 × 0.31
Saturation regime of peak pressure values at focus						
p_0, MPa	1.8	2.15	2.4	0.9	0.925	0.95
I_0, W/cm^2	109	156	194	27.3	28.5	30.5
W_0, W	368	535	686	92	98	108
$p/p_-/A_s$, MPa at focus	113/–27/136	145/–35/175	180/–42/220	106/–23/126	133/–27/156	166/–33/195
Dimensions of focal region p_+/p_- along axes $z \times r$ in mm, level –6 dB	3.9 × 0.27/ 4.6 × 0.73	3.3 × 0.24/ 3.7 × 0.68	2.2 × 0.20/ 2.9 × 0.59	1.98 × 0.14/ 2.7 × 0.42	1.46 × 0.13/ 2.17 × 0.37	1.08 × 0.11/ 1.72 × 0.34

ture transducers with acoustic power of 50 W at 4 MHz and 15 W at 7 MHz are sufficient.

The saturation threshold for the peak positive pressure at the focus occurs at sufficiently high power levels—namely 368, 535, and 686 W for transducers with f_1 = 4 MHz and F = 20, 18, 16 mm, respectively—which are difficult to achieve under practical conditions. For the higher operating frequency of f_2 = 7 MHz, the saturation threshold occurs at lower power levels of 92, 98, and 108 W, respectively. In this case, the focal shock amplitudes differ by approximately 10% between 4 and 7 MHz frequencies: 136, 175, and 220 MPa for f_1 = 4 MHz compared to 126, 156, 195 MPa for f_2 = 7 MHz at F = 20, 18, and 16 mm, respectively. Thus, for transducers with identical apertures, the characteristic nonlinear focusing regimes (quasi-linear distortion, fully developed shocks, and saturation) are achieved at higher acoustic powers in sources with shorter focal lengths than in longer focal-length sources, while the resulting peak pressures and shock amplitudes are also higher [7]. In addition, with an increase in the operating frequency of the transducers, the powers corresponding to the thresholds of

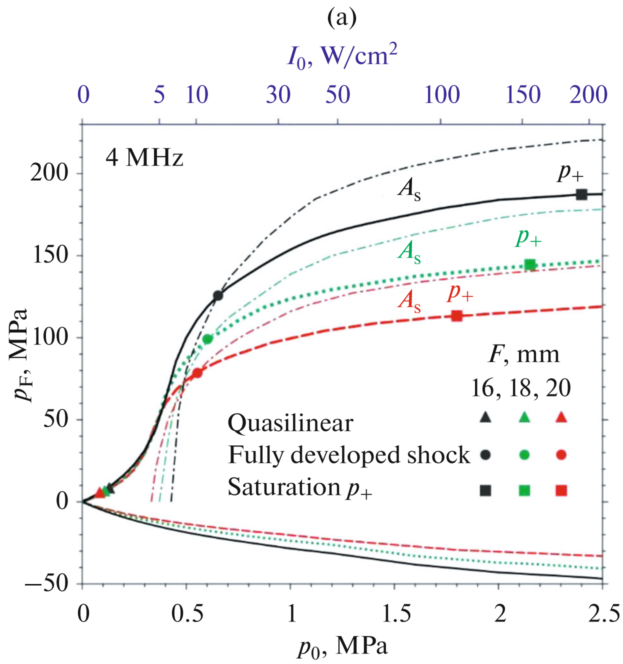

Fig. 4. Dependences of the peak positive and negative pressures, as well as shock amplitude at the focus (saturation curves) on the initial pressure amplitude (lower scale) and intensity (upper scale) for transducers with frequency of (a) 4 and (b) 7 MHz. Solid curves correspond to the transducer with $F_1 = 16$ mm; dotted curve, with $F_2 = 18$ mm; and dashed curve, with $F_3 = 20$ mm.

these three regimes, taking into account the correction for stronger absorption, decrease inversely proportional to the square of the frequency ratio. However, the focal peak pressures and shock amplitudes themselves decrease insignificantly (less than 15% with a change in f from 4 to 7 MHz) due to stronger absorption at high frequencies. Similar trends in the behavior of saturation curves when changing the parameter $F\#$ of the transducer were noted earlier in [7] and are explained by shorter dimensions of the focal region, less collinear and, thus, less efficient interaction of the direct and edge waves in the case of transducers with a smaller $F\#$ (i.e., shorter-focus).

The distortion of the focal pressure waveform as nonlinear effects become more pronounced is illustrated in more detail in Fig. 5. Results are presented for transducers with frequencies of 4 MHz (Figs. 5a, 5c, 5e, 5g) and 7 MHz (Figs. 5b, 5d, 5f, 5h) at three focal lengths: $F = 16$, 18, and 20 mm. At the quasi-linear distortion threshold, where 10% of the wave intensity is converted into higher harmonics, the waveform is already asymmetrically distorted, and the peak positive and negative pressures differ in magnitude by a factor of two (Figs. 5a, 5b). As the degree of nonlinear effects increases, this difference becomes more pronounced. By the time 30% of the wave intensity is converted into higher harmonics (Figs. 5c, 5d), the peak pressures p_+ and $|p_-|$ differ by a factor of four, although a fully developed shock has not yet formed.

With a further increase in the acoustic power of the beam and a corresponding progression of nonlinear effects, a shock front begins to form in the upper part of the waveform. As this occurs, the lower boundary of the shock gradually descends towards the region of negative pressures, and the difference between the peak pressures p_+ and $|p_-|$ increases further.

For the modeled transducers, a fully developed shock forms in the focal waveform—with its lower boundary reaching zero pressure (Figs. 5e, 5f)—when half of the wave intensity is converted into higher harmonics. At this stage of nonlinear waveform distortion, the values of p_+ and $|p_-|$ differ by a factor of approximately 5.5. Note the close agreement of the pressure waveforms with a fully developed shock for both operating frequencies of 4 and 7 MHz (Figs. 5e, 5f). The small difference in the shock amplitude resulting from the change in transducer frequency was studied in detail earlier in [7]. Under the saturation regime, a large portion (up to 60%) of the wave intensity is transferred to higher harmonics, and the peak pressures p_+ and $|p_-|$ differ by a factor of four to five. Concurrently, the asymmetry between the positive and negative phases of the wave profile decreases.

As a general trend, for transducers with identical geometry, the focal waveforms at both 4 and 7 MHz are practically identical in shape and peak pressures across each characteristic nonlinear regime. However, the power required to achieve the corresponding regimes—considering the correction for stronger

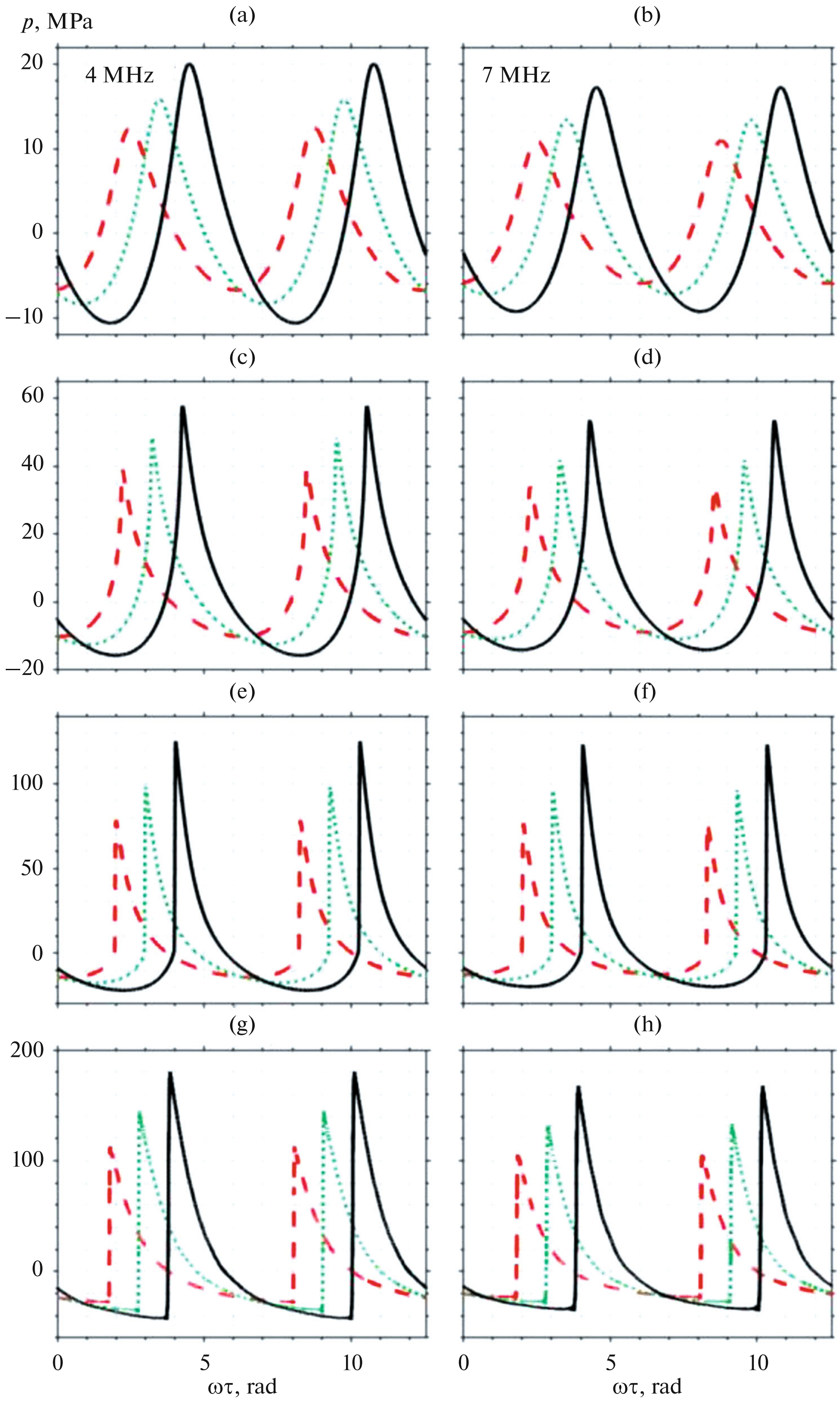

Fig. 5. Pressure waveforms at the focus across characteristic nonlinear focusing regimes: (a, b) quasi-linear distortion, where 10% of wave intensity is converted into higher harmonics; (c, d) stronger nonlinear distortion, where 30% of wave intensity is converted into higher harmonics; (e, f) formation of a fully developed shock, where the shock front reaches zero pressure and approximately 50% of the wave intensity is converted into higher harmonics; and (g, h) saturation of the peak positive pressure. The left column (a, c, e, g) corresponds to a frequency of 4 MHz, and the right column (b, d, f, h) to 7 MHz. Solid, dotted, and dashed curves depict the results for transducers with $F_1 = 16$ mm, $F_2 = 18$ mm, and $F_3 = 20$ mm, respectively. For better clarity, the waveforms are offset by one unit along the abscissa axis.

absorption—is inversely proportional to the square of the frequency ratio; thus, it is significantly lower for higher-frequency transducers. For shorter focal length transducers, with the same degree of manifestation of nonlinear effects, higher absolute levels of peak pressures are observed.

To ensure a comprehensive analysis of the spatiotemporal structure of the nonlinear acoustic fields generated by the modeled transducers, the spatial distributions of the peak positive p_+ and negative p_- pressures along the beam axis were compared. Figure 6 shows the results for the transducers operating at 4 MHz, while Figure 7 presents similar distributions for the higher-frequency radiation (7 MHz). Table 1 lists the dimensions of the focal regions for the peak positive p_+ and negative p_- pressures, defined at the– 6 dB level—analogous to linear beams—for the three characteristic nonlinear focusing regimes.

The results show that at power levels below saturation, nonlinear effects reduce the dimensions of the focal region for the peak positive pressure p_+ compared to those of linear propagation. Conversely, the dimensions of the focal region for the peak negative pressure $p_-$are smallest for a linearly focused beam. In addition, the axial and transverse dimensions of the focal region p_+ have a nonmonotonic dependence on the source power: with increasing power, the dimensions of the focal region p_+ first decrease, reaching a minimum when a shock is formed in the wave profile, and then increase due to a more rapid decrease in the amplitude of the shock near the beam axis (Figs. 6, 7). The dimensions of the focal region of the peak negative pressure p_- increase monotonically as the power of the transducers increases.

Note that for each considered nonlinear focusing regime, the axial size of the p_+ focal region changes more significantly with the transducer F-number than its transverse dimension. In the regime of the fully developed shock, the dimensions of the focal region p_+ along the z and r axes are only 1.3 × 0.18 mm for the short-focus 4 MHz transducer (F_1 = 16 mm) and 2.1 × 0.22 mm for the long-focus transducer (F_3 = 20 mm). When the operating frequency increases to 7 MHz, the corresponding dimensions of the focal region p_+ decrease by approximately 1.8 times, which is slightly higher than the ratio f_2/f_1 = 1.75: 0.7 × 0.1 mm for F_1 = 16 mm and 1.16 × 0.12 mm for F_3 = 20 mm.

It is also worth mentioning the nonmonotonic shift of the maximum p_+ from the geometric focus as the beam power increases: first, with moderate manifestation of nonlinear effects, there is a slight shift of fractions of a millimeter away from the transducer (Figs. 6c, 7c); then, on the contrary, a more noticeable shift towards the transducer (Figs. 6d, 7d); and in saturation regimes (Figs. 6g, 7g) a reverse shift away from the transducer [37, 38]. In this case, the greatest shift of the maximum p_+ from the point of geometric focus, as for linear beams, is observed for longer-focus transducers (Figs. 6, 7). Focal region p_- monotonically shifts towards the transducer as the beam power increases.

Analysis of the behavior of the focusing gain coefficients p_+/p_0 shows the following dynamics: first, the focusing efficiency increases due to the increase in the focusing efficiency of higher harmonics arising in the beam and the difference in the diffraction phase shifts between these harmonics, and then, after the formation of a shock front in the wave profile, the efficiency decreases due to the absorption of energy at the shock fronts formed before the focus. In the case of quasilinear beam focusing, the gain factors p_+/p_0 are approximately 1.5 times higher than the corresponding values p_+/p_0 in the linear case (see Table 1). In the regime of fully developed shock, the gain coefficient p_+/p_0 at the focus increases by 3.2–3.3 times for transducers with an operating frequency of 4 MHz and by 3.4–3.5 times for transducers with a frequency of 7 MHz compared to the values in the linear beam. In the saturation regime, the gain factors at focus p_+/p_0 become comparable to the values observed in the case of quasi-linear beam focusing.

Conversely, the $|p_-|/p_0$ ratio at the focus decreases monotonically with increasing beam power. Thus, in the quasi-linear waveform distortion regime, the $|p_-|/p_0$ values are 1.3 times lower than the corresponding linear gain values for both operating frequencies. In case of the fully developed shock formation regime, the focal $|p_-|/p_0$ ratios are 1.7 times lower than those in the linear beam for an operating frequency of 4 MHz and 1.8 times lower for a frequency of 7 MHz. In the saturation regime, the $|p_-|/p_0$ ratio at the focus for the modeled transducers is approximately three times lower than the values in the linear beam.

In conclusion of the analysis of the spatial structure of the acoustic fields of the transducers considered in this study, Figs. 8 and 9 show two-dimensional distributions of the peak positive (Fig. 8) and peak negative pressures (Fig. 9) for the most interesting case from a practical point of view, namely, the formation of a fully developed shock at the focus. It is clearly seen that the distribution p_+ is very narrow in the transverse direction: only about 0.2 mm for transducers with a frequency of 4 MHz and 0.1 mm for transducers with a higher frequency of 7 MHz (Fig. 8). Such a small width of the focal region p_+ in the transverse directions is comparable to the size of the FOPH fiber in experiments, which makes the experimental characterization of shock-wave fields of miniature high-frequency transducers technically challenging [6].

Focal regions of the peak negative pressures p_- have a cigar-shaped form (Fig. 9) and are significantly larger in size than both the focal regions in the case of linear focusing (Fig. 3) and the corresponding focal regions of the peak positive pressures in nonlinear

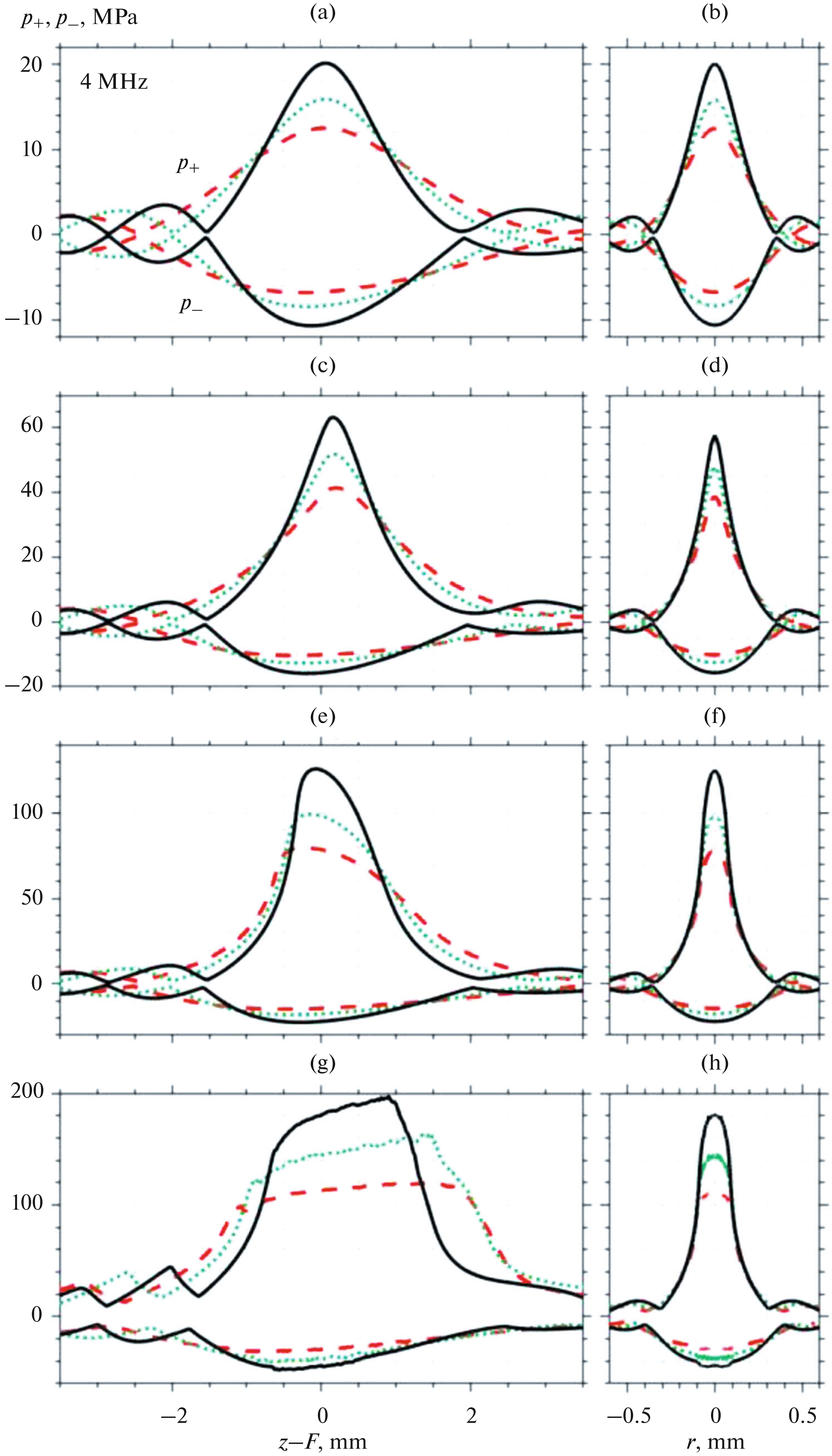

Fig. 6. Spatial axial (a, c, e, g) and focal (b, d, f, h) distributions of the peak positive and negative pressures for 4-MHz transducers across characteristic nonlinear focusing regimes: (a, b) quasi-linear propagation; (c, d) nonlinear propagation; (e,f) formation of a fully developed shock; (g, h) saturation of the peak positive pressure. Solid, dotted, and dashed curves depict results for transducers with $F_1 = 16$ mm, $F_2 = 18$ mm, and $F_3 = 20$ mm, respectively.

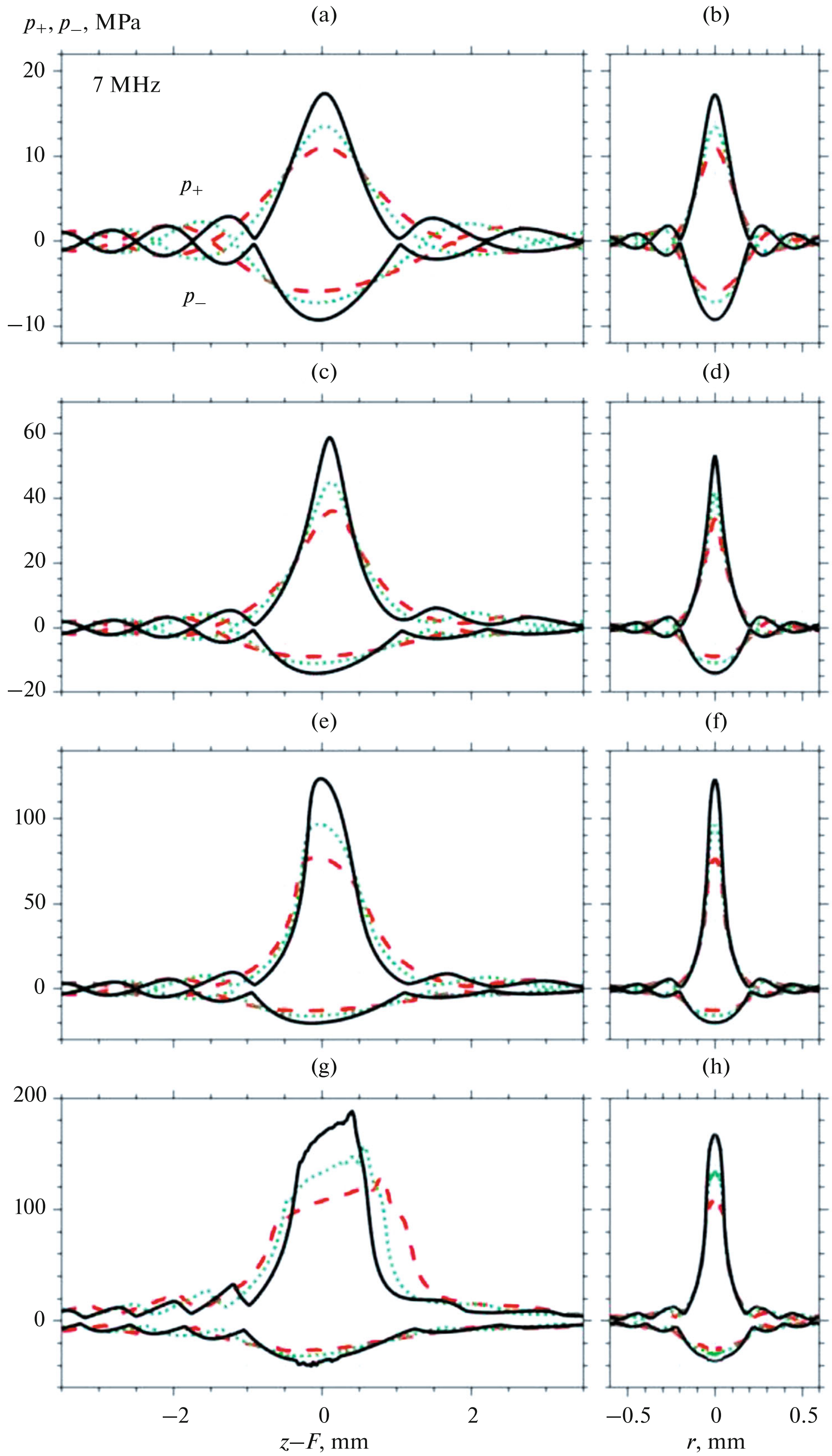

Fig. 7. Spatial axial (a, c, e, g) and focal (b, d, f, h) distributions for the peak positive and negative pressures for 7-MHz transducers across characteristic nonlinear focusing regimes: (a, b) quasi-linear propagation; (c, d) nonlinear propagation; (e, f) formation of a fully developed shock; (g, h) saturation of the peak positive pressure. Solid, dotted, and dashed curves depict results for transducers with $F_1 = 16$ mm, $F_2 = 18$ mm, and $F_3 = 20$ mm, respectively.

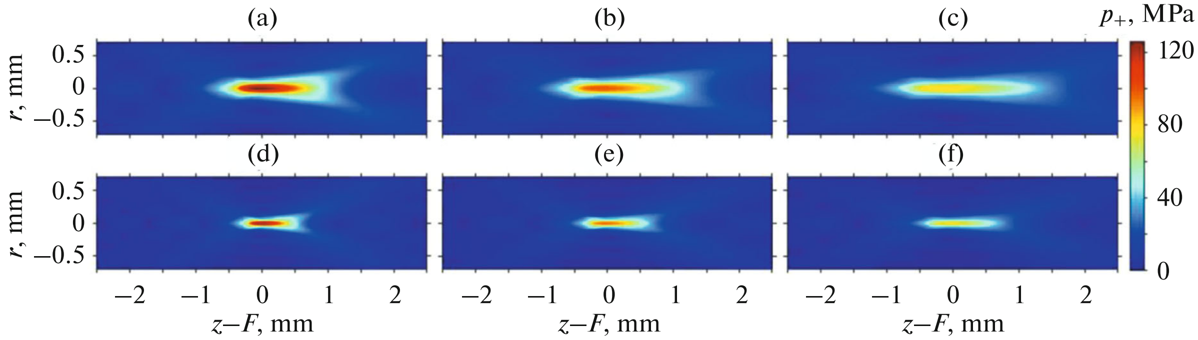

Fig. 8. Two-dimensional distributions of the peak positive pressure in the axial plane in water for the regime of fully developed shock formation at the focus for transducers operating at (a–c) 4 and (d–f) 7 MHz with focal lengths of (a, d) F_1 = 16 mm, (b, e) F_2 = 18 mm, and (c, f) F_3 = 20 mm.

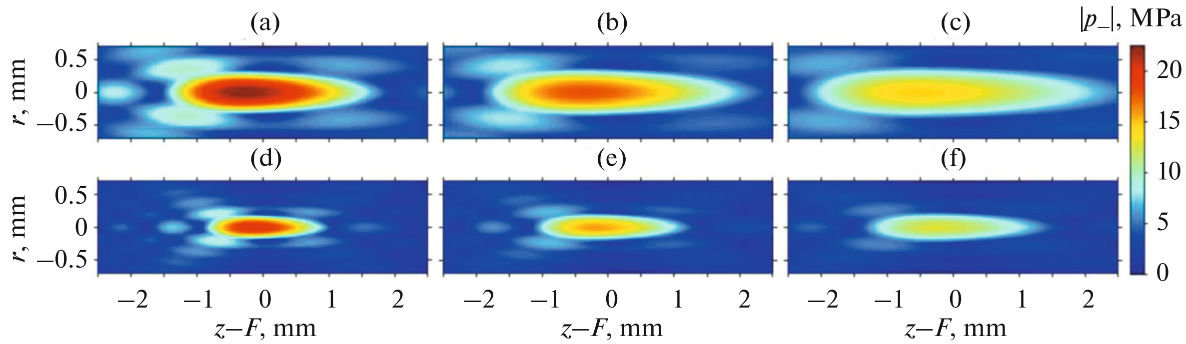

Fig. 9. Two-dimensional distributions of the absolute value of the peak negative pressure in the axial plane in water for the regime of fully developed shock formation at the focus for transducers operating at (a–c) 4 and (d–f) 7 MHz with focal lengths (a, d) F_1 = 16 mm, (b, e) F_2 = 18 mm, and (c, f) F_3 = 20 mm.

beams (Fig. 8). A shift in focal region p_- from the geometric focus towards the transducer (Fig. 9) is clearly observed; however, the magnitude of the shift does not exceed 0.5 mm.

Thus, when utilizing the transducers considered here in practical applications in the regime of fully developed shock formation, one should account for both the reduction in the dimensions of the p_+ focal region and the corresponding expansion of the p_- focal region, as well as the potential shift of the p_+ and $|p_-|$ field maxima from the geometric focus.

Estimation of Acoustic Field Parameters in Biological Tissue

The first step in certifying medical therapeutic ultrasound devices to ensure their effectiveness and safety is to provide calibration data in water. Recently, significant attention has been paid to the use of numerical methods, which complement and sometimes surpass the accuracy of physical experiments [6, 15]. Accordingly, the primary results characterizing the acoustic parameters of nonlinear fields in this work were obtained and analyzed for the case of focusing in water. For clinical applications, knowledge of the achievable field parameters in situ—specifically, at a given focal depth in tissue where physical measurements are typically unfeasible—is necessary. Nonlinear derating methods allow scaling of the initial transducer pressure, intensity, and power to compensate for differences in the absorption and nonlinear properties of water and tissue. This scaling ensures that the same degrees of nonlinear distortion of the wave profile, peak pressure values, and shock amplitudes are achieved at the focus in tissue as in the calibration measurements or modeling in water.

In terms of applying shock-wave focusing regimes to treat superficial skin layers, the most promising focusing regime appears to be the one involving fully developed shock formation at the focus. For exposures at characteristic depths of 4.5 mm at 4 MHz and 3 mm at 7 MHz, and accounting for the differences in absorption, nonlinearity parameter, sound speed, and density between water and skin, Eq. (5) yields estimates of the required transducer powers to achieve this regime.

For transducers with a frequency of 4 MHz and focal lengths F = 20, 18, and 16 mm, this requires powers of 80, 96, and 116 W, while the amplitudes of the fully developed shock at the focus are 85, 107, and 136 MPa, respectively (in water the power is 34, 42, and 50 W and the shock amplitudes are 78, 99, and 126 MPa). For a higher frequency of 7 MHz, powers of 25, 31, and 38 W are required, and the shock amplitudes are close in magnitude (in water, the power is 9.6, 11.9, and 14.6 W and the shock amplitudes are 77, 96, and 123 MPa).

CONCLUSIONS

This paper presents computer models of miniature ultrasound transducers with geometries and frequencies characteristic of noninvasive surgery and therapy for superficial skin layers. A numerical experiment was conducted to investigate the feasibility of implementing shock-wave focusing regimes in water and at characteristic depths in skin, and the required transducer powers were determined. It is shown that for focusing in water, shock amplitudes of up to 120 MPa can be achieved in the focal waveform at powers up to 50 W for 4-MHz transducers (2 cm diameter, 16–20 mm radius of curvature) and up to 15 W for similar 7-MHz transducers. For focusing in tissue at depths of 3–4.5 mm, the corresponding powers are 116 W and 38 W, which are achievable with existing devices; in this case, the shock amplitude reaches 130 MPa. Thus, using numerical modeling, this study demonstrates the feasibility of implementing shock-wave exposures on superficial skin layers for clinical applications, including aesthetic medicine, dermatology, and scar treatment in plastic surgery.

FUNDING

The study was supported by the Russian Science Foundation, grant no. 25-12-00157.

CONFLICT OF INTEREST

The authors of this work declare that they have no conflicts of interest.

REFERENCES

1. W. Feng, G. ter Haar, and I. Rivens, *Image-Guided Focused Ultrasound Therapy: Physics and Clinical Applications* (CRC Press, 2024).
2. Z. Xu, T. D. Khokhlova, C. S. Cho, and V. A. Khokhlova, Annu. Rev. Biomed. Eng. **26**, 141 (2024).
3. R. P. Williams, J. C. Simon, V. A. Khokhlova, O. A. Sapozhnikov, and T. D. Khokhlova, Int. J. Hyperthermia **40** (1), 1 (2023).
4. L. R. Gavrilov, *High Intensive Focused Ultrasound in Medicine* (Fazis, Moscow, 2013) [in Russian].
5. M. R. Bailey, V. A. Khokhlova, O. A. Sapozhnikov, S. G. Kargl, and L. A. Crum, Acoust. Phys. **49** (4), 369 (2003).
6. M. M. Karzova, W. Kreider, A. Partanen, T. D. Khokhlova, O. A. Sapozhnikov, P. V. Yuldashev, and V. A. Khokhlova, IEEE Trans. Ultrason. Ferroelect. Freq. Control **70** (6), 521 (2023).
7. P. B. Rosnitskiy, P. V. Yuldashev, O. A. Sapozhnikov, A. D. Maxwell, W. Kreider, M. R. Bailey, and V. A. Khokhlova, IEEE Trans. Ultrason. Ferroelect. Freq. Control **64** (2), 374 (2017).
8. M. S. Canney, V. A. Khokhlova, O. V. Bessonova, M. R. Bailey, and L. A. Crum, Ultrasound Med. Biol. **36** (2), 250 (2010).
9. T. D. Khokhlova, M. S. Canney, V. A. Khokhlova, O. A. Sapozhnikov, L. A. Crum, and M. R. Bailey, J. Acoust. Soc. Am. **130** (5), 3498 (2011).
10. J. C. Simon, O. A. Sapozhnikov, Y. N. Wang, V. A. Khokhlova, L. A. Crum, and M. R. Bailey, Ultrasound Med. Biol. **41** (5), 1372 (2015).
11. E. Filonenko and V. A. Khokhlova, Acoust. Phys. **47** (4), 468 (2001).
12. P. Ramaekers, M. De Greef, J. M. M. Van Breugel, C. T. W. Moonen, and M. Ries, Phys. Med. Biol. **61** (3), 1057 (2016).
13. P. A. Pestova, P. V. Yuldashev, V. A. Khokhlova, and M. M. Karzova, Acoust. Phys. **70** (3), 434 (2024).
14. F. Wu, Z. B. Wang, W. Z. Chen, W. Wang, Y. Gui, M. Zhang, G. Zheng, Y. Zhou, G. Xu, M. Li, C. Zhang, H. Ye, and R. Feng, Ultrason. Sonochem. **11** (3-4), 149 (2004).
15. C. R. Bawiec, T. D. Khokhlova, O. A. Sapozhnikov, P. B. Rosnitskiy, B. W. Cunitz, M. A. Ghanem, C. Hunter, W. Kreider, G. R. Schade, P. V. Yuldashev, and V. A. Khokhlova, IEEE Trans. Ultrason. Ferroelect. Freq. Control **68** (5), 1496 (2021).
16. J. Vidal-Jove, X. Serres, E. Vlaisavljevich, J. Cannata, A. Duryea, R. Miller, X. Merino, M. Velat, Y. Kam, R. Bolduan, J. Amaral, T. Hall, Z. Xu, F. T. Lee, Jr., and T. J. Ziemlewicz, Int. J. Hyperthermia **39** (1), 1115 (2022).
17. H. J. Laubach, I. R. Makin, P. G. Barthe, M. H. Slayton, and D. Manstein, Dermatol. Surg. **34** (5), 727 (2008).
18. A. M. Al-Jumaily, H. Liaquat, and S. Paul, Ultrasound Med. Biol. **50** (1), 8 (2024).
19. Y. G. Koh, K. R. Kim, Y. H. Lee, H. S. Han, and K. H. Yoo, Med. Lasers **12** (3), 147 (2023).
20. J. A. McGrath, R. A. J. Eady, and F. M. Pope, *Anatomy and Organization of Human Skin* (Blackwell Sci. Ltd., Oxford, 2004).
21. S. R. Thaller, S. Kim, H. Patterson, M. Wildman, and A. Daniller, Plast. Reconstr. Surg. **86** (4), 690 (1990).
22. W. M. White, I. R. Makin, P. G. Barthe, M. H. Slayton, and R. E. Gliklich, Arch. Facial Plast. Surg. **9** (1), 22 (2007).
23. S. G. Fabi, Clin. Cosmet. Investig. Dermatol. **8**, 47 (2015).
24. K. B. Bader, I. R. S. Makin, and J. S. Abramowicz, J. Ultrasound Med. **41** (7), 1597 (2022).
25. A. Ayatollahi, J. Gholami, M. Saberi, H. Hosseini, and A. Firooz, Lasers Med. Sci. **35** (5), 1007 (2020).

26. V. Dicker, L. A. Parra, A. M. Amado, A. Acevedo, D. Castelanich, L. Velasquez, and A. M. Parra, Dermatol. Rev. **6** (2) (2025).
27. J. K. Woodacre, T. G. Landry, and J. A. Brown, IEEE Trans. Ultrason. Ferroelect. Freq. Control **65** (11), 2131 (2018).
28. M. G. Mallay, T. G. Landry, and J. A. Brown, Ultrasonics **139** (2), 107275 (2024).
29. R. R. Fasakhov, A. A. Bogov, and M. R. Zhuravlev, Aspir. Vestn. Povolzh'ya **22** (1), 43 (2022).
30. S. Houshian, S. S. Jing, C. Chikkamuniyappa, G. H. Kazemian, and M. Emami-Moghaddam-Tehrani, J. Hand Surg. Am. **38** (8), 1651 (2013).
31. O. V. Bessonova, V. A. Khokhlova, M. S. Canney, M. R. Bailey, and L. A. Crum, Acoust. Phys. **56** (3), 354 (2010).
32. P. V. Yuldashev and V. A. Khokhlova, Acoust. Phys. **57** (3), 334 (2011).
33. N. Bilaniuk and G. S. K. Wong, J. Acoust. Soc. Am. **93** (3), 1609 (1993).
34. P. V. Yuldashev, M. M. Karzova, W. Kreider, P. B. Rosnitskiy, O. A. Sapozhnikov, and V. A. Khokhlova, IEEE Trans. Ultrason. Ferroelect. Freq. Control **68** (9), 2837 (2021).
35. https://itis.swiss/virtual-population/tissue-properties/database/acoustic-properties/.
36. F. A. Duck, *Physical Properties of Tissue* (Acad. Press, London, 1990).
37. O. V. Bessonova, V. A. Khokhlova, M. R. Bailey, M. S. Canney, and L. A. Crum, Acoust. Phys. **55** (4–5), 463 (2009).
38. M. M. Karzova, M. V. Aver'yanov, O. A. Sapozhnikov, and V. A. Khokhlova, Acoust. Phys. **58** (1), 81 (2012).